

# Modelling the spinning dust emission from LDN 1780

Matias Vidal <sup>1</sup>, <sup>1</sup>★ Clive Dickinson <sup>2</sup>, S. E. Harper, <sup>2</sup> Simon Casassus <sup>3</sup> and A. N. Witt <sup>4</sup>

<sup>1</sup>Universidad Autónoma de Chile, Facultad de Ingeniería, Núcleo de Astroquímica & Astrofísica, Av. Pedro de Valdivia 425, Providencia, Santiago, Chile

<sup>2</sup>Jodrell Bank Centre for Astrophysics, Alan Turing Building, School of Physics and Astronomy, The University of Manchester, Oxford Road, Manchester M13 9PL, UK

<sup>3</sup>Departamento de Astronomía, Universidad de Chile, Casilla 36-D, Santiago, Chile

<sup>4</sup>Ritter Astrophysical Research Center, University of Toledo, Toledo, OH 43606, USA

Accepted 2020 April 21. Received 2020 April 18; in original form 2019 September 12

## ABSTRACT

We study the anomalous microwave emission (AME) in the Lynds Dark Nebula (LDN) 1780 on two angular scales. With publicly available data at an angular resolution of  $1^\circ$ , we studied the spectral energy distribution of the cloud in the 0.408–2997 GHz frequency range. The cloud presents a significant ( $>20\sigma$ ) amount of AME, making it one of the clearest examples of AME on  $1^\circ$  scales, and its spectrum can be well fitted with a spinning dust (SD) model. We also find at these angular scales that the location of the peak of the emission at lower frequencies (23–70 GHz) differs from the location at the higher frequencies (90–3000 GHz) maps. In addition to the analysis on  $1^\circ$  angular scales, we present data from the Combined Array for Research in Millimeter-wave Astronomy (CARMA) at 31 GHz with an angular resolution of 2 arcmin, in order to study the origin of the AME in LDN 1780. We studied morphological correlations between the CARMA map and different infrared tracers of dust emission. We found that the best correlation is with the 70- $\mu\text{m}$  template, which traces warm dust ( $T \sim 50$  K). Finally, we study the difference in radio emissivity between two locations within the cloud. We measured a factor of  $\approx 6$  difference in 31-GHz emissivity. We show that this variation can be explained, using the SD model, by a variation on the dust grain size distribution across the cloud, particularly changing the fraction of polycyclic aromatic hydrocarbon for a fixed total amount of carbon.

**Key words:** radiation mechanisms: general – ISM: clouds – dust, extinction – ISM: individual objects: LDN 1780 – photodissociation region (PDR) – radio continuum: ISM.

## 1 INTRODUCTION

The *WMAP* (Bennett et al. 2013) and *Planck* (Planck Collaboration I 2011a) satellites, as a byproduct of the making of cosmic microwave background (CMB) maps, have provided precise full-sky maps of the different diffuse emission mechanisms on the Galaxy. Among them is the anomalous microwave emission (AME), first detected by Leitch et al. (1997) as a correlation between dust emission at 100  $\mu\text{m}$  from IRAS and 14.5-GHz radio emission toward the north celestial pole, which could not be accounted for by synchrotron or free-free emission.

In our Galaxy, AME can account for up to 30 per cent of the diffuse emission at 30 GHz (Planck Collaboration XIII 2016c; Planck Collaboration XXV 2016d). AME is present in a variety of astrophysical environments, namely molecular clouds (MCs; Finkbeiner et al. 2002; Watson et al. 2005; Casassus et al. 2006, 2008; AMI Consortium et al. 2009; Dickinson et al. 2010), translu-

cent clouds (Vidal et al. 2011), reflection nebulae (Castellanos et al. 2011), H II regions (Dickinson et al. 2007, 2009; Todorović et al. 2010), and in the galaxies NGC 6946, NGC 4725 (Murphy et al. 2010, 2018), and M31 (Battistelli et al. 2019). AME may also be important in compact objects like protoplanetary discs (PPDs). Hoang et al. (2018) predicted that AME from spinning silicates or polycyclic aromatic hydrocarbons (PAHs) dominates over thermal dust emission at frequencies  $<60$  GHz in PPDs, even in the presence of significant dust growth, and Greaves et al. (2018) reproduced the AME they detect in two discs using a model in which hydrogenated nanodiamonds were the spinning carriers. For an up-to-date review on AME, refer to Dickinson et al. (2018).

AME is the least-understood emission mechanism in the 1–100 GHz range as its study have been difficult due to the diffuse nature of the emission. While it has been clearly detected by CMB experiments and telescopes at  $\sim 1^\circ$  angular resolution, there are only a handful of detections higher angular resolutions (e.g. Scaife et al. 2010; Tibbs et al. 2011; Battistelli et al. 2015). This has made the identification of the AME carriers and also their physical properties

\* E-mail: [matias.vidal@autonoma.cl](mailto:matias.vidal@autonoma.cl)

difficult. Currently, we only know some general properties of AME, like being associated with photodissociation regions (PDRs). AME is thought to be caused by dust grains, possessing electric dipole moments, spinning at GHz frequencies. This is an old idea that was first proposed by Erickson (1957).

The spinning dust (SD) hypothesis has been preferred by the observations and the more convincing examples are the Perseus and  $\rho$  Ophiuchi MCs (Watson et al. 2005; Casassus et al. 2008; Planck Collaboration XX 2011b). Detailed theoretical models have been developed that predict the SD spectrum for different types of grains and different astrophysical environments (Draine & Lazarian 1998; Ali-Haïmoud, Hirata & Dickinson 2009; Hoang, Draine & Lazarian 2010; Silsbee, Ali-Haïmoud & Hirata 2011; Ysard, Juvela & Verstraete 2011; Hoang & Lazarian 2012). Contrasting the observations with these models gives us the opportunity to study the microphysics of the ISM from a new window at GHz frequencies, in particular the behaviour of the smallest dust grains.

Nevertheless, some doubt has been cast on the SD paradigm by Hensley, Draine & Meisner (2016), who found that the *Planck* AME map is uncorrelated with a template of PAH emission. PAHs are thought to be one of the main carriers of AME in the SD model, so their results show that much research is still needed in this area.

Here we present 31 GHz data from the Combined Array for Research in Millimeter-wave Astronomy (CARMA) of the Lynds Dark Nebula (LDN) 1780, a high Galactic latitude ( $l = 359^\circ.0$ ,  $b = 36^\circ.7$ ) translucent region at a distance of  $110 \pm 10$  pc (Franco 1989). LDN 1780 has a moderate column density (a few  $\times 10^{21}$  cm $^{-2}$ ) that corresponds to the ‘translucent cloud’ type of object, i.e. interstellar clouds with some protection from the radiation field, with optical extinctions in the range  $A_V \sim 1\text{--}4$  mag (Snow & McCall 2006). Using an optical-depth map constructed from ISO 200- $\mu$ m observations, Ridderstad et al. (2006) found a mass of  $\sim 18 M_\odot$  and reported no young stellar objects based on the absence of colour excess in point sources.

LDN 1780 is a known source of AME. Vidal et al. (2011) detected AME from this cloud through observations at 31 GHz. They found that the AME at 31 GHz correlates best with the IRAS 60- $\mu$ m map, which traces hot and small dust grains. This correlation was even tighter than with an 8  $\mu$ m, which traces PAH. Here we revisit this cloud, using archival data to study the spectral energy distribution (SED) at  $1^\circ$  angular scales. We also use our CARMA data in addition to IR and sub-mm templates to study and model the AME on angular scales of 2 arcmin.

In Section 2, we describe the CARMA observations, as well as the ancillary data used in the analysis. Section 3 describes the SED of the cloud on  $1^\circ$  angular scales. Section 4 corresponds to the analysis at a 2-arcmin resolution based on the CARMA data. Section 5 concludes.

## 2 DATA

### 2.1 CARMA data

We obtained 31-GHz data from CARMA Sunyaev–Zel’dovich Array (SZA). The array has eight antennas of 3.5-m diameter, with six ‘inner’ telescopes arranged in a compact configuration (baselines ranging from 4.5 to 11.5 m) and two telescopes provide longer baselines of 56 and 78 m. The observing frequency band corresponds to the 26–36 GHz range, with a primary beam of  $\approx 10.5$ -arcmin full width at half-maximum (FWHM) at 31 GHz.

We observed a three pointings mosaic centred at the peak of the 31-GHz emission as observed by the Cosmic Background Imager

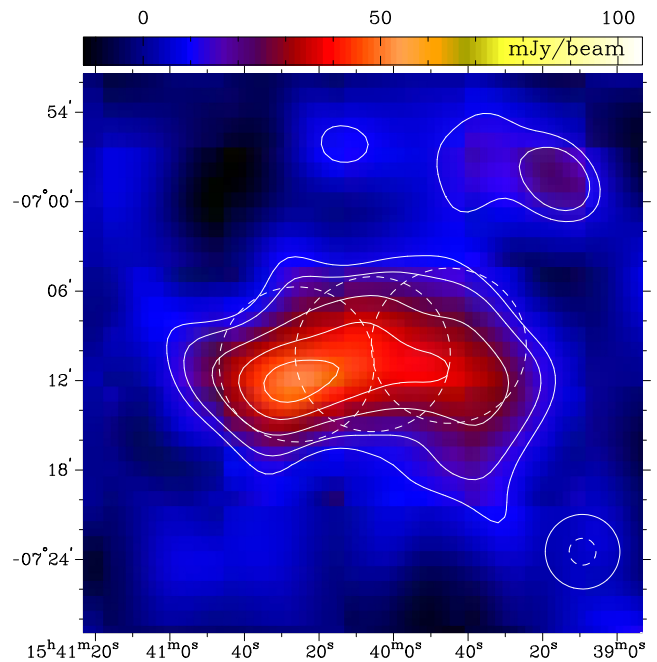


**Figure 1.** 31-GHz map observed by the Cosmic Microwave Imager (CBI), from Vidal et al. (2011). The dashed lines show the position of the three pointings observed by CARMA, with a diameter indicating the primary beam of the CARMA antennas of 10.5 arcmin. The two circles at the bottom right-hand panel represent the synthetic beams of the CBI (5.4 arcmin) and CARMA (1.8 arcmin).

(CBI) in Vidal et al. (2011). Fig. 1 shows the location of the three pointings, drawn on top of the CBI 31-GHz map of the cloud, from Vidal et al. (2011).

### 2.2 Observations

The observations were performed in two epochs, the first one between 2012 June 9 and July 21, and the second one between 2013 May 19 and June 14. Each run is divided into small observations blocks (OBs). The total observing time adds up to 25.2 h. During each one of the OBs, the source is observed along with three calibrators, namely flux calibrator (3C 273), passband calibrator (1337–129), and phase calibrator (1512–090). The OB consisted of observations of the flux calibrator during 5 min, then the observation of the passband calibrator during 5 min, followed by the target cycle where the phase calibrator is observed during 3 min, followed by 15 min on source.

We calibrated the data using the MIRIAD data-reduction package (Sault, Teuben & Wright 1995). We performed a small amount of flagging to remove particularly noisy combinations of baselines and spectral channels.

### 2.3 Imaging

To image the calibrated visibilities, we used the CLEAN (e.g. Högbom 1974) method and also the MEM (e.g. Cornwell & Evans 1985) reconstruction. This was done to identify any possible imaging artefact of the extended emission. In order to maximize the signal-to-noise ratio (S/N) in the restored image, we chose natural weights.

In the maps there are two radio sources listed in Condon et al.’s (1998) catalogue. We measured their flux at 31 GHz and also the

**Table 1.** Point sources subtracted from the visibilities.

NVSS name	$S_{1.4\text{ GHz}}$ (mJy)	$S_{31\text{ GHz}}$ (mJy)	$\alpha_{1.4/31}$
J154006–070442	$25.8 \pm 1.3$	$3.5 \pm 1.2$	$-0.64 \pm 0.26$
J154024–070858	$13.3 \pm 0.6$	$6.2 \pm 1.3$	$-0.25 \pm 0.16$

*Notes.* The location and 1.4-GHz fluxes are from Condon et al.’s (1998) catalogue. The 31-GHz fluxes were obtained from our CARMA observations.

spectral index between 1.4 and 31 GHz. Table 1 list the location and measured values. As we are only interested in the diffuse emission from the cloud, we subtracted the two sources directly from the visibilities. This was done by first using CLEAN to obtain their flux density. An appropriate point model is then subtracted from the visibilities. Table 1 also lists our measured coordinates and flux densities at 31 GHz. We inspected the subtracted maps after to check for artifacts in case of a bad estimation of the flux. Any residual from the source subtraction is smaller than the rms noise of the maps.

We used Gaussian ( $u, v$ ) tapering as a way to improve the sensitivity to the more extended emission. This has the effect of downweighting the longer baselines, degrading the final angular resolution of the map from  $\sim 1.6$  arcmin to a final resolution of 2 arcmin. An added advantage of smoothing CARMA data to the 2-arcmin resolution is that it symmetrizes the beam.

After imaging with both methods, MEM and CLEAN, the rms noise in the MEM map is 40 per cent lower than the noise in the CLEAN (0.99 and 1.4 mJy beam $^{-1}$ , respectively). Fig. 2 shows both maps and they present a similar morphology, although the MEM reconstruction seem to recover more of the extended and diffuse emission. Because of this, we chose to use the MEM map for the rest of the analysis.

## 2.4 Ancillary data

Besides the CARMA data, we also used ancillary data to study the cloud. We constructed a SED from 0.408 GHz to 2997 GHz on a 1 $^\circ$  angular scale using the data listed in Table 2.

Remazeilles et al. (2015) re-processed the 0.408-GHz map of Haslam et al. (1982). The new map is available at the LAMBDA website,<sup>1</sup> includes the point sources and has an effective resolution of 56 arcmin. We also used the 1.42-GHz map from Reich (1982), Reich & Reich (1986), and Reich et al. (2001) with an angular resolution of 36 arcmin and the the 2.326-GHz map from Jonas et al. (1998), which has an angular resolution of 20 arcmin. We assumed a 10 per cent uncertainty in these three data sets. An additional uncertainty of 0.8 K is added to the 0.408-GHz map, in order to account for the striations on the map as measured in Remazeilles et al. (2015).

From 23 to 94 GHz, we included the five WMAP 9-yr maps (Bennett et al. 2013) at 1 $^\circ$  resolution. They present a 0.2 per cent calibration uncertainty. We decided to use a more conservative 4 per cent uncertainty in order to account for any additional errors due to non-symmetric beams, and any colour correction effect.

Between 28 and 857 GHz, we used the *Planck* temperature maps released in 2015 (PR2) (Planck Collaboration I 2016a), available in the Planck Legacy Archive.<sup>2</sup>

<sup>1</sup><http://lambda.gsfc.nasa.gov/>

<sup>2</sup><http://pla.esac.esa.int/pla/>

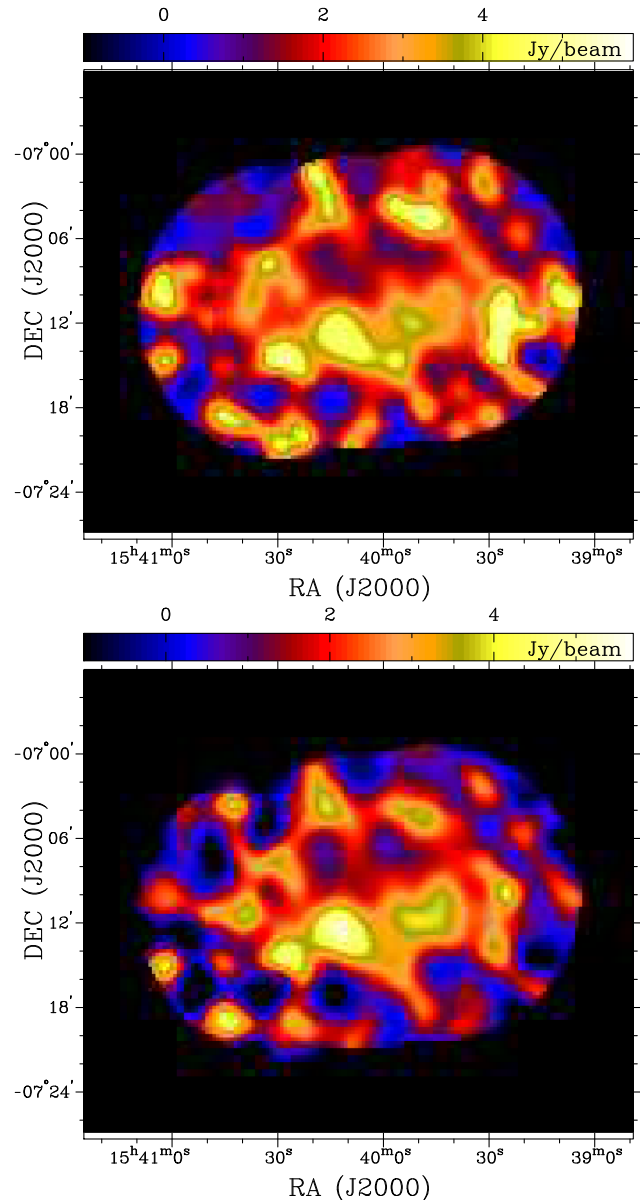


**Figure 2.** Top panel: CLEAN mosaic reconstruction of the data after the  $uv$  tapering, in order to increase the sensitivity to extended emission. The rms noise of the map is 4 mJy beam $^{-1}$ . Bottom panel: MEM mosaic reconstruction, with a rms noise of 0.99 mJy beam $^{-1}$ . The synthesized beam size is plotted as an ellipse at the bottom right-hand corner of both maps. It has a size of 2-arcmin FWHM, and a beam size of 2 arcmin.

## 3 SED AT 1 $^\circ$ RESOLUTION

### 3.1 Photometry

First, we converted all maps from antenna temperature units into flux units (Jy pixel $^{-1}$ ) with the following relationship:

$$S = \frac{2k T_{RJ} \nu^2 \Omega_{\text{pix}}}{c^2}, \quad (1)$$

where  $\Omega_{\text{pix}}$  represents the pixel solid angle,  $T_{RJ}$  is the brightness temperature,  $\nu$  the observing frequency,  $k$  the Boltzmann constant, and  $c$  the speed of light (see Planck Collaboration XX 2011b; Planck Collaboration XI 2013a, for a similar analysis on other sources).

**Table 2.** List of ancillary data used in the analysis.

Telescope/survey	Freq. (GHz)	Nominal resolution (arcmin)	Reference
Haslam	0.408	56.0	Haslam et al. (1982), Remazeilles et al. (2015)
Reich	1.42	35.4	Reich (1982), Reich & Reich (1986), Reich, Testori & Reich (2001)
Jonas	2.3	20.0	Jonas, Baart & Nicolson (1998)
WMAP 9-yr	22.8	51.3	Bennett et al. (2013)
Planck	28.4	32.3	Planck Collaboration I (2016a)
WMAP 9-yr	33.0	39.1	Bennett et al. (2013)
WMAP 9-yr	40.7	30.8	Bennett et al. (2013)
Planck	44.1	27.1	Planck Collaboration I (2016a)
WMAP 9-yr	60.7	21.1	Bennett et al. (2013)
Planck	70.4	13.3	Planck Collaboration I (2016a)
WMAP 9-yr	93.5	14.8	Bennett et al. (2013)
Planck	100	9.7	Planck Collaboration I (2016a)
Planck	143	7.3	Planck Collaboration I (2016a)
Planck	217	5.0	Planck Collaboration I (2016a)
Planck	353	4.8	Planck Collaboration I (2016a)
Planck	545	4.7	Planck Collaboration I (2016a)
Planck	857	4.3	Planck Collaboration I (2016a)
COBE-DIRBE	1249	37.1	Hauser et al. (1998)
COBE-DIRBE	2141	38.0	Hauser et al. (1998)
COBE-DIRBE	2997	38.6	Hauser et al. (1998)

Flux densities are obtained integrating on a circular aperture of  $2^\circ$  in diameter centred at the cloud. To estimate the uncertainty of the fluxes, we measured the median value of the pixels within a ring, extending from 80 to 100 arcmin away from the centre.

Fig. 3 shows  $20\ 1^\circ$  resolution maps of the cloud, ranging from 0.408 up to 2997 GHz. Over plotted on each map is the aperture used for the photometry. At frequencies above 217 GHz, the thermal dust emission from LDN 1780 can be detected clearly over the background. At intermediate frequencies (23–143 GHz), the maps are dominated by CMB emission. In the low-frequency maps (0.408–2.3 GHz), there is no clear emission at the location of the cloud that rises above the background level.

At  $1^\circ$  angular scales, the contribution of the CMB has been very well mapped by the *Planck* and *WMAP* missions. We subtracted a CMB map (the SMICA map from Planck Collaboration IX 2016b) to each of the individual maps. After this, the emission from the cloud is clearly visible from 23 up to 2997 GHz. The CMB-subtracted maps are shown in Fig. 4. Note that the position of the peak changes slightly among some of the maps (e.g. *WMAP* 23 GHz, *Planck* 545 GHz). We will discuss this later in Section 3.3.

The maps in Fig. 4 between 40 and 70 GHz show some additional structure around the cloud. We quantify this by measuring the standard deviation of the fluctuations within a ring between  $1^\circ$  and  $3^\circ$  from the centre of the cloud. Table 3 lists the measured standard deviation values for the CMB-subtracted maps at 44 GHz, 60 GHz and 70 GHz. The second column lists the rms noise values of each of each map. The rms noise accounts for more than  $\sim 50$  per cent of the standard deviation that we measured in the ring aperture. The residual fluctuations can be due to uncertainties in the CMB map. In order to estimate the uncertainty coming from the CMB template, we measured the fluctuations on the four CMB maps that were produced by the *Planck* team: Commander, NILC, SEVEM, and SMICA (Planck Collaboration IX 2016b). The average value for the fluctuations around LDN 1780 is  $5.6\ \mu\text{K}$ , which can be used as a measurement of the uncertainty of the CMB maps around the cloud. This value, in addition with the rms noise value of the maps, accounts for

the fluctuations that we measured in the 40-, 60-, and 70-GHz maps.

Table 4 lists the measured flux densities. Also listed are the flux densities in the CMB-subtracted maps.  $2\ \sigma$  upper limit are given for the three lowest frequencies as they present negative fluxes.

### 3.2 SED fitting

At these frequency ranges, the continuum emission components are five: thermal dust, AME, CMB, free–free, and synchrotron emission. Due to the low flux densities present at the lowest frequencies (see Table 4), we decided to not include a synchrotron component. Therefore, we model the SED using four components:

$$S = S_{\text{ff}} + S_{\text{AME}} + S_{\text{CMB}} + S_{\text{TD}}. \quad (2)$$

The  $\text{H}\alpha$  line is commonly used as a tracer of free–free emission, provided that the line is the result of *in situ* recombination. There is some  $\text{H}\alpha$  emission coming from the cloud, but Witt et al. (2010) showed that most of it consists of scattered light from the diffuse  $\text{H}\alpha$  component of the Galactic interstellar radiation field (ISRF). We define a conservative upper limit for the free–free component, using the estimated value at 31 GHz over a  $1^\circ$  scale of  $S_{31} = 0.09\ \text{Jy}$  from Vidal et al. (2011), which was calculated using the  $\text{H}\alpha$  map from the SHASSAA survey (Gaustad et al. 2001).

We extrapolate this value to other frequencies using

$$S_{\text{ff}} = S_{31} (\nu/31\ \text{GHz})^{\beta_{\text{ff}}}, \quad (3)$$

with a free–free spectral index  $\alpha_{\text{ff}} = -0.13$ , valid for the diffuse ISM (Draine 2011).

A SD model is used to account for the AME component. We used the SPDUST package (Ali-Haïmoud et al. 2009; Silsbee et al. 2011), which calculates the SD emissivity for a population of grains,  $j_\nu$ , in units of the hydrogen column density. It models the spectrum using a number of physical parameters. We used the parameters for the ‘warm neutral medium’ (WNM), defined in Draine & Lazarian (1998), which produce an spectrum that peaks at 23.6 GHz. By fitting for the amplitude of this generic spectrum, we only have one

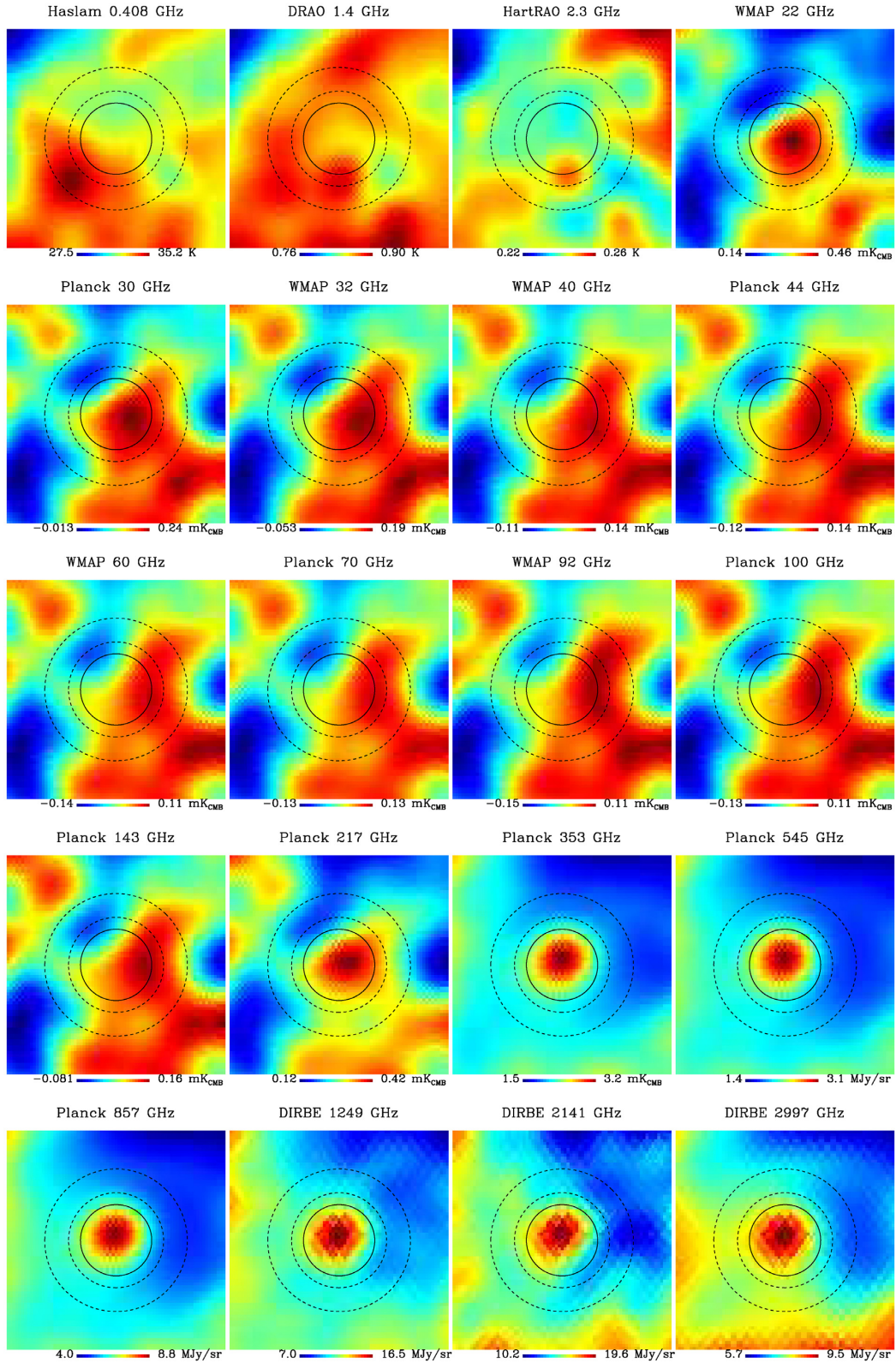


**Figure 3.**  $5^\circ \times 5^\circ$  multi-frequency maps of LDN 1780 from 0.408 up to 2997 GHz. All maps have been smoothed to  $1^\circ$  FWHM and have a linear colour scale. Overplotted on each map is the aperture and annulus used in the aperture photometry.

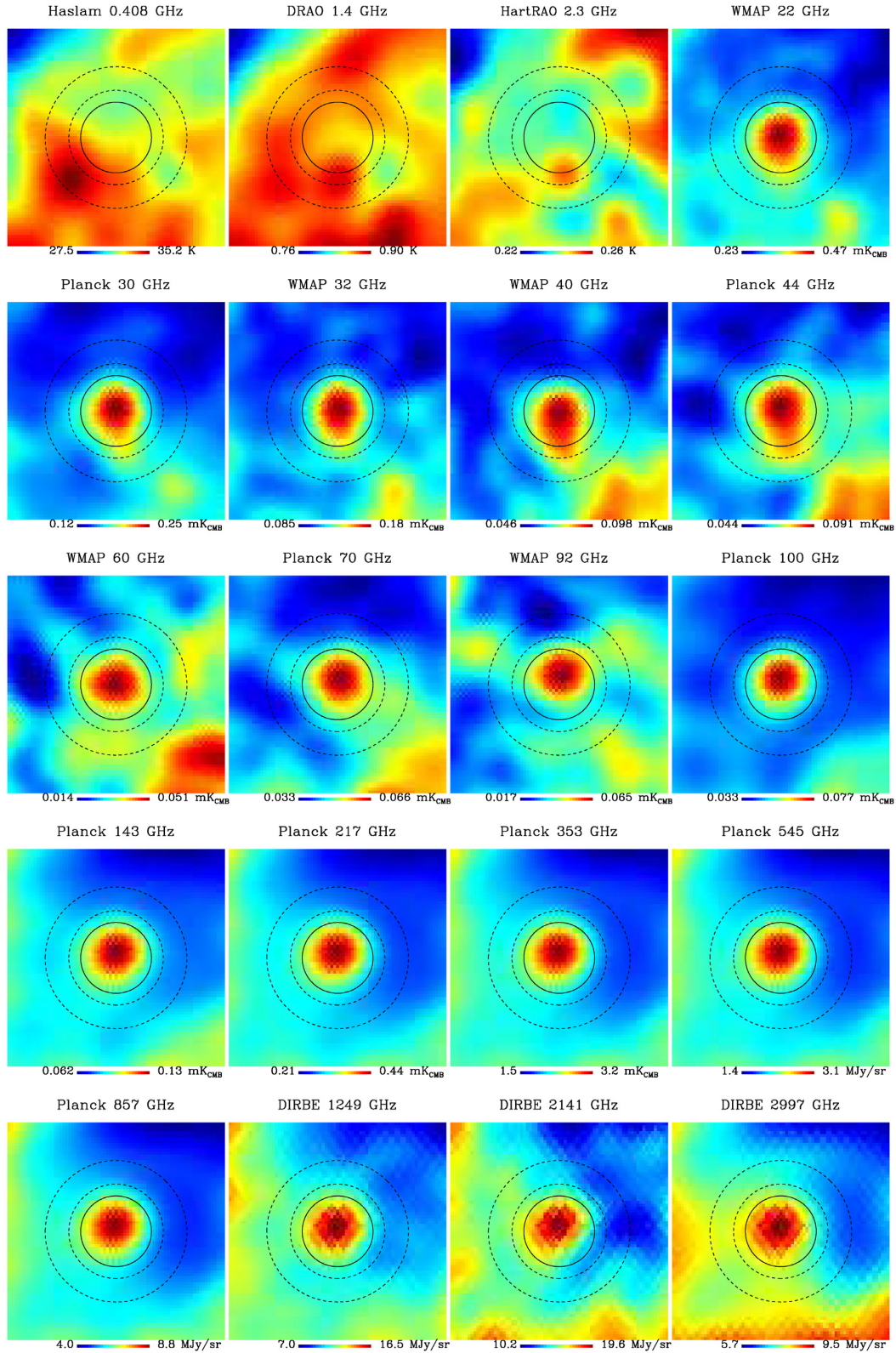


**Figure 4.**  $5^\circ \times 5^\circ$  multi-frequency CMB-subtracted maps of LDN 1780 from 0.408 up to 2997 GHz. All maps have been smoothed to  $1^\circ$  FWHM and have a linear colour scale. Overplotted on each map is the aperture and annulus used in the aperture photometry. Note the difference with the maps shown in Fig. 3, specially in the range 23–217 GHz, which is dominated by CMB emission.

**Table 3.** List of measurements of the standard deviation of the fluctuations around the source in the of the 44-, 60-, and 70-GHz CMB-subtracted maps shown in Fig. 4.

Map	Standard deviation ( $\mu\text{K}$ )	rms noise ( $\mu\text{K}$ )
<i>Planck</i> 44 GHz	12.0	5.9
<i>WMAP</i> 60 GHz	7.6	4.7
<i>Planck</i> 70 GHz	7.0	4.3

Note. Also listed in the second column are the r.m.s noise values.

**Table 4.** Aperture photometry flux densities of LDN 1780.

Survey	Frequency (GHz)	Flux density (Jy)	CMB-sub flux density (Jy)
Haslam	0.4	<2.2	<2.2
DRAO	1.4	<0.14	<0.14
HartRao	2.3	<0.12	<0.12
<i>WMAP</i>	23	$1.4 \pm 0.05$	$1.1 \pm 0.06$
<i>Planck</i>	30	$1.6 \pm 0.09$	$1.1 \pm 0.07$
<i>WMAP</i>	33	$1.3 \pm 0.10$	$0.8 \pm 0.08$
<i>WMAP</i>	41	$1.4 \pm 0.16$	$0.8 \pm 0.11$
<i>Planck</i>	44	$1.5 \pm 0.18$	$0.8 \pm 0.12$
<i>WMAP</i>	61	$1.7 \pm 0.33$	$0.7 \pm 0.22$
<i>Planck</i>	70	$2.8 \pm 0.42$	$1.4 \pm 0.27$
<i>WMAP</i>	93	$3.9 \pm 0.70$	$1.7 \pm 0.48$
<i>Planck</i>	100	$5.5 \pm 0.72$	$3.0 \pm 0.45$
<i>Planck</i>	143	$10.8 \pm 1.1$	$6.5 \pm 0.79$
<i>Planck</i>	217	$33.8 \pm 1.4$	$27.8 \pm 1.6$
<i>Planck</i>	353	$123 \pm 2$	$124 \pm 4$
<i>Planck</i>	545	$407 \pm 10$	$407 \pm 13$
<i>Planck</i>	857	$1151 \pm 31$	$1151 \pm 40$
DIRBE	1249	$1860 \pm 62$	$1860 \pm 81$
DIRBE	2141	$1639 \pm 83$	$1639 \pm 108$
DIRBE	2997	$749 \pm 35$	$749 \pm 46$

free parameter,  $A_{\text{sd}}$ , that describes the SD component. Section 4.3 provides more details on the SPDUST modelling.

The CMB component is defined using the differential form of a blackbody at  $T_{\text{CMB}} = 2.726 \text{ K}$  (Fixsen 2009):

$$S_{\text{CMB}} = \left( \frac{2k v^2 \Omega}{c^2} \right) \Delta T_{\text{CMB}}, \quad (4)$$

where  $\Delta T_{\text{CMB}}$  is the anisotropy temperature of the CMB in thermodynamics units.

A modified blackbody model is usually used to describe the thermal emission from dust at wavelengths  $\lambda > 60 \mu\text{m}$ . It has the form

$$S_{\text{TD}} = 2h \frac{v^3}{c^2} \frac{1}{e^{h\nu/kT_d} - 1} \tau_{250} (v/1.2 \text{ THz})^{\beta_d} \Omega, \quad (5)$$

with  $k$ ,  $c$ , and  $h$  the Boltzmann constant, the speed of light, and the *Planck* constant, respectively; the dust temperature is  $T_d$  and the optical depth at  $250 \mu\text{m}$  is  $\tau_{250}$ .

Two of the *Planck* bands, the ones centred at 100 and 217 GHz, might include an important contribution from CO line emission (*Planck* Collaboration XIII 2013b; transitions  $J = 1 \rightarrow 0$  at 115 GHz and  $J = 2 \rightarrow 1$  at 230 GHz). We decided not to include the two mentioned band in the SED fit in order to avoid any CO contamination the flux measurements as LDN 1780 has a known molecular component (Laureijs et al. 1995).

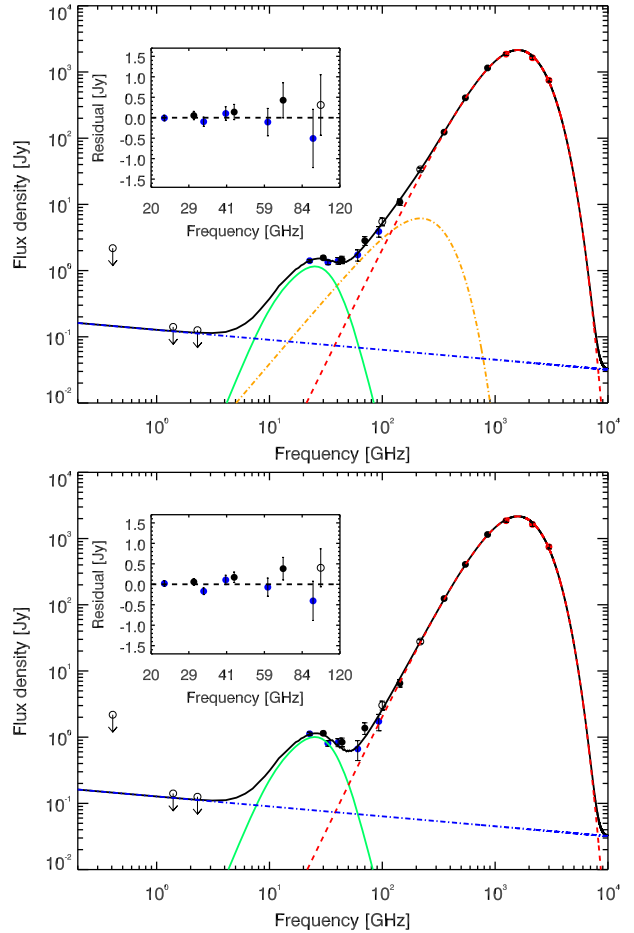


**Figure 5.** Spectra of LDN 1780 using the flux densities measurements listed in Table 4. The best fit to the data is the black lines that correspond to the sum of four components. Thermal dust emission in red dashed line and CMB in orange. The blue line is an upper limit for the free–free emission estimated from  $H\alpha$  emission. The SD component is plotted in green. The *Planck* points at 10 and 217 GHz that can be contaminated with CO emission are not used in the fit and shown with an empty circle. In the inset, we show the residuals (i.e. data–model) in the spectral range of where the SD emission is significant. In the bottom panel is the SED measured with the CMB-subtracted maps.

To calculate the non-linear least-squares fit, we used the MPFIT IDL package (Markwardt 2009), which uses the Levenberg–Marquardt algorithm. The top panel of Fig. 5 shows the SED from 0.408 to 2997 GHz and the the best fit to the data using the model from equation (2), and the bottom panel shows the best fit to the CMB-subtracted data. In both plots, the low-frequency data are represented with  $2\sigma$  upper limits. The largest uncertainty at 0.408 GHz comes from the  $\pm 0.8 \text{ K}$  striations measured by Remazeilles et al. (2015). The blue triangle at 23 GHz represents the expected free–free level predicted by the *WMAP* MEM map (Bennett et al. 2013). A small CO contribution can be seen at 100 and 217 GHz in the CMB-subtracted SED; however, its flux is less than 10 per cent at 100 GHz. Being such at small effect at 100 and 217 GHz means that it will be negligible at 353 GHz, so it is safe that we have use the 353-GHz map in our SED. Table 5 lists the fitted parameters and its uncertainties.

Note in Table 5 the small difference in the fitted parameters between the normal and the CMB-subtracted maps, which is consistent with zero within the uncertainties. The CMB amplitude

**Table 5.** Parameters, uncertainties, and reduced  $\chi^2$  value from the SED fit over  $1^\circ$  scales.

Parameter	Normal	No CMB
$\tau_{250} (\times 10^{-5})$	$2.1 \pm 0.2$	$2.2 \pm 0.3$
$T_d$ (K)	$17.1 \pm 0.4$	$16.9 \pm 0.5$
$\beta_d$	$1.5 \pm 0.1$	$1.5 \pm 0.1$
$A_{sd} (10^{20} \text{ cm}^{-2})$	$2.4 \pm 0.1$	$2.0 \pm 0.1$
$\Delta T_{\text{CMB}}$ ( $\mu\text{K}$ )	$13.3 \pm 1.7$	$2.3 \pm 1.3$
$\chi_r^2$	0.9	1.9

*Note.* In the second column are listed the fit parameters for the CMB-subtracted maps. Fig. 5 shows the two SEDs.

in the CMB-subtracted fit is also consistent with zero. This shows consistency between the two fits. The fit using the CMB-subtracted maps shows a higher  $\chi_r^2$ . One reason for this is the smaller error bars of the data points. The uncertainties of the aperture photometry are calculated by measuring the fluctuations within the annular ring, and in the case without CMB, they are much smaller. There is a significant contribution from the CMB in this cloud at angular scales  $\sim 1^\circ$ , but as we see from the fit, it is well constrained.

The two SEDs show that this cloud presents a significant amount of AME. If we fix the SD component of the fit to zero, we obtain an extremely poor overall fit to the CMB-subtracted maps, with  $\chi_r^2 = 40$ . The case when we include the SD component has  $\chi_r^2 = 1.9$ . The amplitude of the SD component is  $A_{sd} = 2.4 \pm 0.1$  and  $2.0 \pm 0.1$  for the original and CMB-subtracted maps, respectively. This corresponds to a significance of  $24\sigma$  and  $20\sigma$ , respectively, making LDN 1780 one of the clearest examples of AME on  $1^\circ$  angular scales. In the analysis by Planck Collaboration XV (2013c), LDN 1780 was not detected as an AME source. We believe that the reason is that LDN 1780 does not appear as a conspicuous source in the original maps, and only shows clearly after subtracting a CMB template, as its location is coincident with a high value of the CMB anisotropy.

Another important aspect to highlight is the lack of emission from the cloud in the low-frequency maps ( $\nu \leq 2.3$  GHz). This means that LDN 1780 is a rising spectrum source at  $\nu > 5$  GHz.

### 3.3 Peak location

If we take a closer look to Fig. 4, we can notice that the location of the peak of the cloud in the lower frequencies (23–70 GHz) is very close to the centre of the aperture. On the other hand, the cloud appears shifted north by a few arcmin in the higher frequency maps (93–2997 GHz). In order to measure this shift, we measured the position of the peak of the cloud in all the maps from 23 to 2997 GHz using SEXTRACTOR (Bertin & Arnouts 1996). Table 6 list the location and uncertainties for the peak of the emission for all the maps between 23 and 2997 GHz. In Fig. 6, we plot these values using coloured ellipses on top of the 250- $\mu\text{m}$  *Herschel* map orientated in Galactic coordinates, where the *blue* ellipses correspond to the maps from 22.8 to 60.7 GHz, and the *red* ellipses to the maps from 70.4 to 2997 GHz. The averaged position is also plotted as a filled ellipse.

The location of the low-frequency (22.8–60.7 GHz) peak is closer to the peak of the IR emission originated from small grains (e.g. 8  $\mu\text{m}$ , 12  $\mu\text{m}$ ). This is most interesting as it is what is expected from the SD model. Moreover, this is also along the direction of the local radiation field that illuminates the cloud, which comes from the Galactic plane direction (Witt et al. 2010). We will now explore further this morphological correlation using the CARMA data.

**Table 6.** Location of the peak of the cloud for *WMAP*, *Planck*, and *DIRBE* maps in Galactic coordinates.

Map	Gal. lon. ( $^\circ$ )	Gal. lat. ( $^\circ$ )
DIRBE 2997	$359.19 \pm 0.02$	$36.63 \pm 0.02$
DIRBE 2141	$359.17 \pm 0.02$	$36.67 \pm 0.01$
DIRBE 1249	$359.17 \pm 0.02$	$36.61 \pm 0.02$
<i>Planck</i> 857	$359.17 \pm 0.02$	$36.62 \pm 0.02$
<i>Planck</i> 545	$359.18 \pm 0.03$	$36.63 \pm 0.03$
<i>Planck</i> 353	$359.17 \pm 0.03$	$36.63 \pm 0.03$
<i>Planck</i> 217	$359.17 \pm 0.07$	$36.63 \pm 0.06$
<i>Planck</i> 143	$359.16 \pm 0.13$	$36.61 \pm 0.13$
<i>Planck</i> 100	$359.13 \pm 0.15$	$36.60 \pm 0.15$
<i>WMAP</i> 93.5	$359.07 \pm 0.19$	$36.76 \pm 0.17$
<i>Planck</i> 70.4	$359.10 \pm 0.19$	$36.35 \pm 0.25$
Averaged	$359.077 \pm 0.002$	$36.635 \pm 0.002$
<i>WMAP</i> 60.7	$359.22 \pm 0.22$	$36.48 \pm 0.17$
<i>Planck</i> 44.1	$359.16 \pm 0.15$	$36.46 \pm 0.17$
<i>WMAP</i> 40.7	$359.12 \pm 0.12$	$36.16 \pm 0.17$
<i>WMAP</i> 33	$359.05 \pm 0.08$	$36.41 \pm 0.11$
<i>Planck</i> 28.4	$359.13 \pm 0.08$	$36.42 \pm 0.08$
<i>WMAP</i> 22.8	$359.11 \pm 0.05$	$36.44 \pm 0.07$
Averaged	$359.13 \pm 0.04$	$36.43 \pm 0.05$

*Note.* We also list the averaged values for the maps in the ranges 70.4–2997 and 22.8–60.7 GHz.

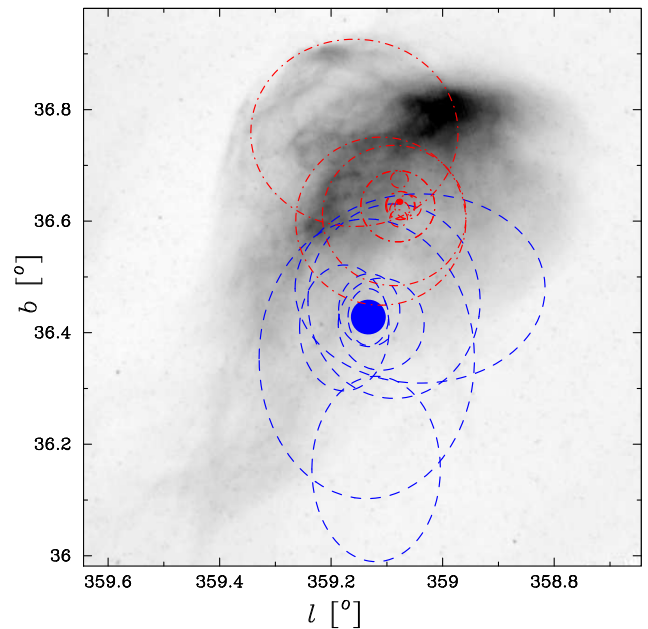


**Figure 6.** Ellipses centred at the location of the peak of the cloud for the *WMAP*, *Planck*, and *DIRBE* maps. The size of the ellipses represent  $1\sigma$  uncertainties, taken from Table 6. In *blue* are shown the frequencies between 22.8 and 60.7 GHz while in *red* the maps from 70.4 to 2997 GHz. The filled ellipses correspond to the averaged values shown also in Table 6. On grey scale is the 250- $\mu\text{m}$  *Herschel* map of LDN 1780 in Galactic coordinates.

## 4 PROPERTIES OF DUST AT 2-ARCMIN RESOLUTION

The ESA *Herschel* Space Observatory (Pilbratt et al. 2010) provided maps with angular resolution better than  $\sim 35$  arcsec at 70, 160, 250, 350, and 500  $\mu\text{m}$ . We used these maps to calculate physical properties of the cloud at 2-arcmin angular resolution, similar to

our CARMA observations. We fitted the thermal dust emission (equation 5) in each pixel to obtain the dust temperature and the optical depth ( $\tau_{250}$ ). As we have less data points than in the  $1^\circ$  SED fit (5 versus 20), we decided to fix the spectral index of the modified blackbody to  $\beta_d = 1.6$ . This value is similar to the one we found in the  $1^\circ$  SED and consistent with the measurements by *Planck* of the diffuse ISM (Planck Collaboration XI 2013a). We calculated the fit only for the pixels that have a S/N greater than 2. Fig. 7 shows the resulting optical depth at 250  $\mu\text{m}$  and dust temperature maps. Colder areas occur at the regions with larger optical depth, as they are more protected from the ISRF.

The optical depth map can be used to estimate the hydrogen column density, using the relation measured by Planck Collaboration XXV (2011c),  $\tau_{250}/N_{\text{H}} = 2.32 \pm 0.3 \times 10^{-25} \text{ cm}^2$ . We can also calculate the intensity of the radiation field,  $G_0$ , based on the dust temperature map, using the relation from Ysard, Miville-Deschênes & Verstraete (2010):

$$G_0 = \left( \frac{T_d}{17.5 [\text{K}]} \right)^{\beta_d+4}, \quad (6)$$

where the radiation field has a spectral distribution with a standard shape, as defined by Mathis, Mezger & Panagia (1983). We note however that Planck Collaboration IX (2013a) has shown that this relation might not be true in every environment, as the variations observed in  $T_d$  would be due to changes in dust properties (e.g. grain size distribution or grain structure) instead of the intensity of the ISRF. Nevertheless, we will use the maps we calculated in the following section.

#### 4.1 IR correlations

Here we investigate morphological correlations between the 31-GHz emission as seen by CARMA and IR tracers. We include *Spitzer*-IRAC map at 8  $\mu\text{m}$ , which traces primarily PAHs, as well as the *Spitzer*-MIPS map at 24  $\mu\text{m}$ , tracing primarily VSGs. Similar analyses can be found in the literature and they show different results in different types of clouds and in different angular scales. Scaife et al. (2010) found in the LDN 1246 cloud that the 8- $\mu\text{m}$  *Spitzer* map was the closest to their 16-GHz observations. Casassus et al. (2006) and Tibbs et al. (2011) reported better correlations between radio data and 60  $\mu\text{m}$ . On large areas of the sky, the *Planck* team finds that the FIR map correlates better with the AME template (Planck Collaboration XXV 2016d). On LDN 1780, Vidal et al. (2011) found that the 31-GHz data from the CBI was closer to IRAS 60  $\mu\text{m}$ . Using a full-sky analysis, Hensley et al. (2016) found that, on average, the best correlation of AME is with the dust radiance map.

Here we selected a rectangular area of  $25 \times 15 \text{ arcmin}^2$  at the centre of the CARMA mosaic where we calculate the spatial correlations. All maps were smoothed to a common angular resolution of 2 arcmin (the same as the CARMA map at 31 GHz). In order to quantify the level correlation between two maps, we chose the Spearman's rank correlation coefficient,  $r_s$ , which has the advantage over the more commonly used Pearson correlation coefficient, and works also for non-linear variables. When  $r_s = 1$ , it means that the two quantities are monotonically related. We estimated uncertainties for  $r_s$  using 1000 Monte Carlo simulations, which were generated from the uncertainties in the maps.

We measured  $r_s$  between the CARMA data at 31 GHz and different IR templates at 8, 24, 70, 160, 250, 350, and 500  $\mu\text{m}$ . The IR emission from the smallest dust grains depends directly on the intensity of the radiation field. Because of this, we also measured

$r_s$  with the IR templates divided by the  $G_0$  map ( $G_0 \propto T_d^{5.6}$ ), in order to account for the variation in the ISRF across the cloud. In other words, the IR maps corrected by  $G_0$  are better tracers of the column density of the emitting grains than the native maps.

Table 7 list  $r_s$  for the different native IR templates, the maps corrected by  $G_0$  and also the ratio between these values. Among the native maps, the best correlation is with 70  $\mu\text{m}$  template. The worst correlations are with the NIR maps at 8 and 24  $\mu\text{m}$ . The 160-, 250-, 350-, and 500-  $\mu\text{m}$  maps show a similar  $r_s$ . This is expected as they all trace emission from the same population of larger grains that are in thermodynamic equilibrium with the radiation field. When correcting by the  $G_0$  map, the  $r_s$  value improves by a factor of 2–3 for the 8- and 24-  $\mu\text{m}$  maps. This increment in the correlation is significant and can even be appreciated by eye. Fig. 8 shows the native 8-, 24-, 70-, and 160-  $\mu\text{m}$  maps of the cloud on the left-hand panel, and the maps corrected by  $G_0$  on the right-hand panel. The contours of the 31-GHz emission are drawn in black. Note that the  $G_0$ -corrected 8- and 24-  $\mu\text{m}$  maps show a morphology more similar to the 31-GHz contours. The correlation with the longer wavelength maps ( $\geq 70 \mu\text{m}$ ) degrades, but not significantly after the  $G_0$  correction.

The fact that the correlation improves significantly (by a factor of 2.7 and 2.2; see Table 7) after the correction for the radiation field illumination of the small grains, traced both by the 8- and 24-  $\mu\text{m}$  maps suggests that the emission seen at 31 GHz might be produced not only by the PAHs (traced by the 8-  $\mu\text{m}$  map) but also by small and warmer grains more exposed to the external radiation field, traced by the 24-  $\mu\text{m}$  map.

#### 4.2 Magnetic dust?

In this work, we are assuming that the emission mechanism responsible for the 31-GHz emission is SD. Another possibility is that the mechanism responsible is *magnetic dust* (Draine & Lazarian 1999; Draine & Hensley 2012; Hoang & Lazarian 2016), where the microwave emission originates from magnetic dipole emission due to thermal fluctuations of the magnetization within individual grains. Here, the main emitters are dust grains that are strongly magnetic, such as metallic iron/nickel, magnetite, and maghemite (Draine & Lazarian 1999) or non-magnetic grains with inclusions of some of these highly magnetic materials. If we assume that there is a population of these ferromagnetic grains and they are well mixed with the rest of the dust components, then the cm-wave emission due to the magnetic dipole should be proportional to the column of dust ( $N_D$ ) and its temperature ( $T_D$ ). Taking a constant dust-to-gas ratio,  $N_D \propto N_{\text{H}}$ . In Fig. 7, we show on the *bottom* panel a colour map displaying the product  $T_D N_{\text{H}}$ , overlaid with the 31-GHz CARMA contours. There is no clear correlation between the radio and the  $T_D N_{\text{H}}$ , which resembles closely the optical depth map from the top panel of Fig. 7. This means that the magnetic dust hypothesis fails to explain the bulk of the 31-GHz emission mapped by CARMA. Moreover, on  $1^\circ$  angular scales, the situation is similar as can be appreciated in Fig. 6, where the peak of the low-frequency (23–60 GHz) maps does not corresponds to the peak of the thermal dust map (250  $\mu\text{m}$ ).

Another prediction of some magnetic dust models is a high degree of polarization. Looking at the *WMAP* *K*-band maps in total intensity and in polarization intensity, we find a polarization fraction  $\Pi = P/I \approx 10$  per cent, with  $P = \sqrt{q^2 + u^2}$  being the naive estimator for the polarization amplitude ( $q, u$  represent the Stokes parameters). Considering the positive bias that affects  $\Pi$  (e.g. Wardle & Kronberg

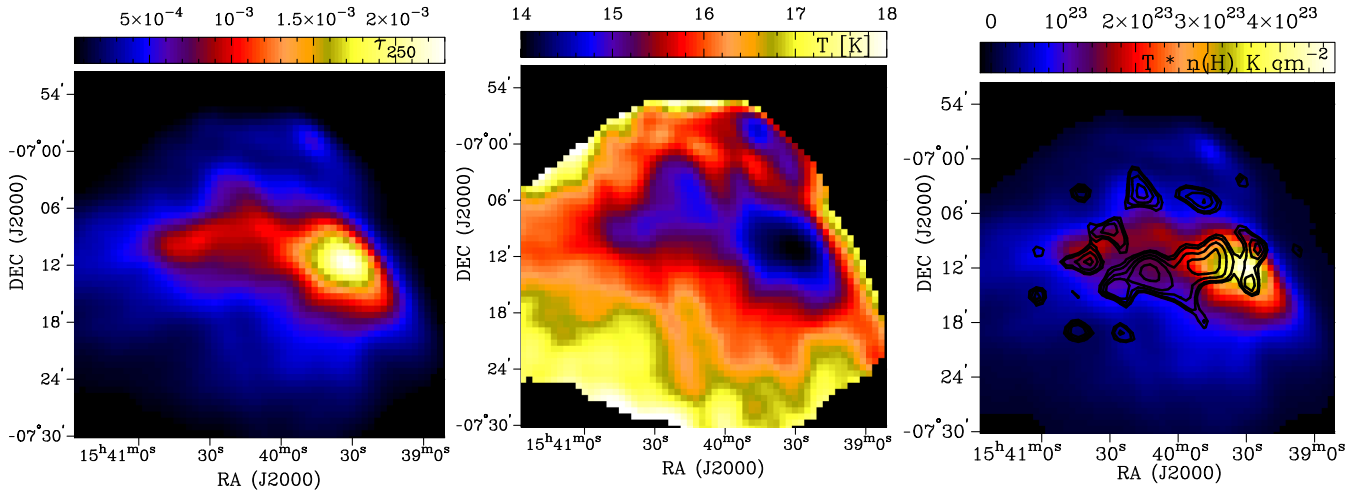


**Figure 7.** Top panel: Optical depth at  $250\ \mu\text{m}$  (left-hand panel) and the dust temperature (right-hand panel) for LDN 1780. The coldest areas of the cloud, at  $T_d \approx 14\ \text{K}$ , correspond to regions with larger optical depth. Bottom panel: Product of the hydrogen column density  $N_{\text{H}}$  and the dust temperature  $T_D$ , with overimposed contours of the 31 GHz CARMA map.

**Table 7.** Correlation values between the 31-GHz map and different IR templates using the Spearman’s rank,  $r_s$ .

Wavelength ( $\mu\text{m}$ )	$r_s$	$r_s[G_0]$	$r_s[G_0]/r_s$
8	$0.14 \pm 0.06$	$0.38 \pm 0.07$	$2.7 \pm 0.5$
24	$0.21 \pm 0.06$	$0.46 \pm 0.06$	$2.2 \pm 0.3$
70	$0.49 \pm 0.07$	$0.45 \pm 0.07$	$0.9 \pm 0.2$
160	$0.36 \pm 0.07$	$0.31 \pm 0.07$	$0.9 \pm 0.3$
250	$0.35 \pm 0.06$	$0.31 \pm 0.07$	$0.9 \pm 0.3$
350	$0.34 \pm 0.06$	$0.30 \pm 0.07$	$0.9 \pm 0.3$
500	$0.34 \pm 0.06$	$0.30 \pm 0.06$	$0.9 \pm 0.3$

*Notes.* The correlation using the maps corrected by the ISRF are shown in the central column ( $r_s[G_0]$ ). The right-hand column list the ration between the quantities in the previous columns.

1974; Montier et al. 2015; Vidal, Leahy & Dickinson 2016), it would set 10 per cent as an upper limit for the polarization intensity at the peak of the cloud. Most MDE models predict higher polarization than this.

### 4.3 SD modelling

We note that the peak of the emission at 31 GHz does not correspond to the region with the larger column density. This means that there is a larger radio emissivity (defined as the measured intensity at 31 GHz per hydrogen column density) from the less dense regions, which can be due to either due to a lack of small grains (e.g. due to coagulation of small grains to big grains) or due to local enhancement of the environmental conditions that trigger the SD emission. We will investigate here if this emissivity variation is consistent with the SD hypothesis.

We will compare the radio emissivity at the peak of the 31 GHz map with the one at the peak of the column density of the cloud. Fig. 9 shows the 31-GHz and the hydrogen column density maps, where we have highlighted these two regions. Table 8 lists the average values measured on a 2-arcmin diameter aperture on the  $N_{\text{H}}$ ,  $T_D$ , and  $G_0$  maps described in Section 4. Also listed are the 31-GHz flux densities in the 2-arcmin aperture and the 31-GHz emissivity in each region.

The 31-GHz emissivity in Region 1 is  $18.7/3.2 = 5.8$  times larger than that of Region 2. We want to test if the SPDUST package from Ali-Haïmoud et al. (2009) and Silsbee et al. (2011) can generate emissivities that differ by a factor of  $\sim 5.8$  within the cloud, with plausible physical conditions.

In the SPDUST package, there are seven input parameters that are related to the environmental conditions of the emitting region. These are as follows:

- (i) total hydrogen number density  $n_{\text{H}}$ ;
- (ii) gas temperature  $T$ ;
- (iii) intensity of the radiation field relative to the average interstellar radiation field  $G_0$ ;
- (iv) hydrogen ionization fraction  $x_{\text{H}} \equiv n_{\text{H}^+}/n_{\text{H}}$ ;
- (v) ionized carbon fractional abundance  $x_{\text{C}} \equiv n_{\text{C}^+}/n_{\text{H}}$ ;
- (vi) molecular hydrogen fractional abundance  $y \equiv 2n(\text{H}_2)/n_{\text{H}}$ ;
- (vii) ‘line’ parameter: it corresponds to the number line number of table 1 of Weingartner & Draine (2001), which lists the parameters that define the grain size distribution.

The SPDUST code has been used by many authors to compare the AME emissivity with radio data. Normally, most parameters are kept fixed to standard values for different astrophysical environments (e.g. CNM, warm ionized medium). Here we would like to constrain the range of some parameters using additional information of the physical conditions in LDN 1780. Different combinations of the SPDUST parameters can produce similar output spectra. Also, some of these parameters are strongly correlated. To tackle these complications, we use an exhaustive approach where we run SPDUST over a grid of parameters, for a total of  $10^7$  runs. Table 9 lists the range and the spacing for each parameter.

From each run of SPDUST, we recover the peak frequency, the peak emissivity, and also the parameters that define a fourth-order polynomial fit to the SPDUST spectrum. The polynomial fit is calculated around the peak of the spectrum. In order to explore the results from the SPDUST runs, we use observational constraints from ancillary sources in some of the physical parameters in LDN 1780.

Mattila & Sandell (1979) used the 100-m Effelsberg telescope to observe the H I and OH lines of the cloud. They measured that the hydrogen kinetic temperature was in the range  $T_{\text{k}} = 40\text{--}56\ \text{K}$  and a total mean density of the gas of  $n = 1.8 \times 10^3\ \text{cm}^{-3}$ . Others works

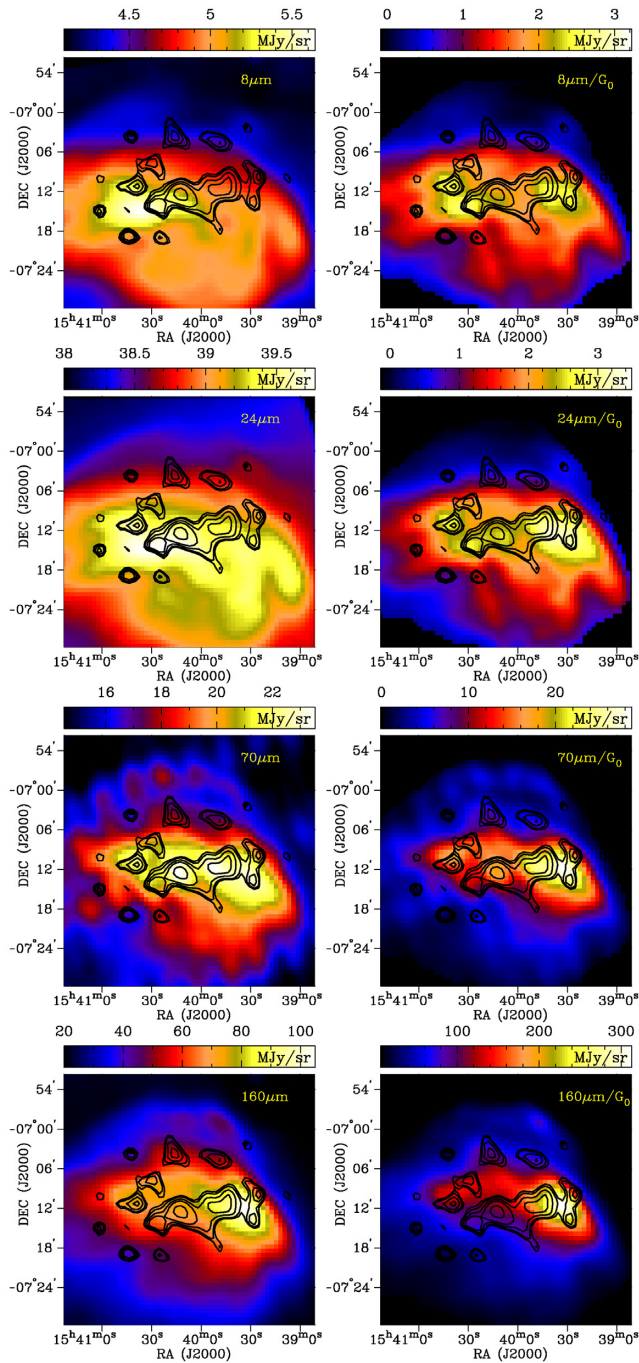


**Figure 8.** 8-, 24-, 70-, and 160- $\mu\text{m}$  maps of LDN 1780. On the left-hand panel column are the native maps and on the right-hand panel, the same maps have been divided by the radiation field template ( $G_0$ ). In each map, we have overlaid the contours of the 31-GHz CARMA map. Table 7 lists the correlation values between the 31-GHz map and the different IR templates.

have measured densities of  $n = 1 \times 10^3$  (Laureijs et al. 1995) and  $0.6 \times 10^3 \text{ cm}^{-3}$  (Toth et al. 1995). Both of these works show also that the cloud is in virial equilibrium, with an  $r^{-2}$  density profile.

We used the previous information to estimate the gas density in the two regions shown in Fig. 9. Giving that the column density at Region 1 is very close to the mean value over the entire cloud (Fig. 9, left-hand panel), we will assume that the gas density at this point is equal to  $1000 \text{ cm}^{-3}$ , the average density of the cloud.

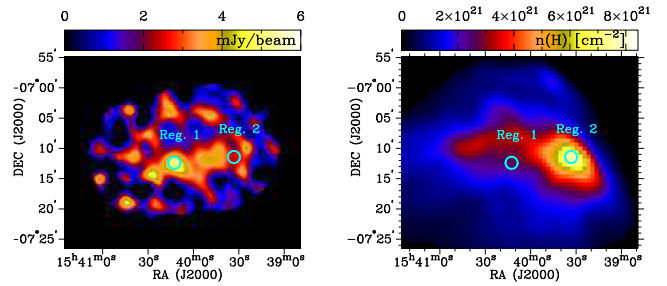


**Figure 9.** Left-hand panel: LDN 1780 as seen by CARMA at 31 GHz. Right-hand panel:  $N_{\text{H}}$  map calculated using IR data in Section 4. The peak of the CARMA map is labelled Region 1, while the peak of the  $N_{\text{H}}$  map is Region 2; both have a diameter of 2 arcmin.

**Table 8.** Physical parameters and integrated fluxes for Regions 1 and 2 defined in Fig. 9.

Region	$N(H)$ ( $\times 10^{21} \text{ cm}^{-2}$ )	$T_{\text{d}}$ (K)	$G_0$	$S_{31}$ (mJy)	$S_{31}/N(H)$ $\times 10^{-24} (\text{Jy cm}^{-2})$
1	2.4	16.6	0.7	4.5	18.7
2	7.3	15.0	0.4	2.4	3.2

*Note.* Hydrogen column density, dust temperature, and radiation field intensity ( $G_0$ ) were obtained in Section 4.

**Table 9.** Range of the parameters used for defining the grid for running SPDUST.

Parameter	Min	Max	Steps	Type
$n_{\text{H}}$	0.1	$10^5$	10	log
$T$	10	$10^5$	10	log
$\chi$	$10^{-4}$	3000	10	asinh
$x_{\text{H}}$	$10^{-4}$	1	10	asinh
$x_{\text{C}}$	$10^{-4}$	1	10	asinh
$y$	$10^{-4}$	1	10	asinh
$b_{\text{c}}$	0	1	10	linear

*Notes.* The parameters are the hydrogen column density, gas temperature, intensity of the radiation field, and hydrogen, carbon, and  $\text{H}_2$  fractional abundances.  $b_{\text{c}}$  quantifies the proportion of PAH grains in the dust.

Region 1 is located about half-way between the peak and the border of the cloud. Giving that the cloud presents an  $r^{-2}$  density profile, the highest density of the cloud (at Region 2) will be  $0.5^{-2} = 4$  times larger than the mean value.

We will assume that the region with higher column density (Region 2) will have the lowest gas temperature, equivalent to  $T = 40 \text{ K}$ , the lower limit of the temperature range measured by Mattila & Sandell (1979). For Region 1, we will assume  $T = 56 \text{ K}$ , the upper limit allowed by Mattila & Sandell's (1979) work. For the ISRF, we take the values from the  $G_0$  map that we produced in Section 4. We note that Region 2 is coincident with the peak of molecular  $^{13}\text{CO}$  gas, observed by Toth et al. (1995), implying that in this region, the ionization fraction will be very close to zero. For Region 1, we use the ionization fraction values defined by Draine & Lazarian (1998) for the cold neutral medium (CNM). We also take the standard values for the carbon ionization fraction and the molecular fraction of hydrogen, defined in Draine & Lazarian (1998) for the CNM and MC environments for Regions 1 and 2, respectively. Table 10 lists all the parameters used for Regions 1 and 2, as well as the standard values defined in Draine & Lazarian

**Table 10.** Physical parameters used in SPDUST for Regions 1 and 2 (see Fig. 9).

Region	$n(H)$ ( $\text{cm}^{-3}$ )	$T$ (K)	$G_0$	$x_H$	$x_C$	$y$	'line' WD2001
MC	300	20	0.01	0	0.0001	0.99	7
CNM	30	100	1	0.0012	0.0003	0	7
Reg 1	1000	56	0.7	0.0012	0.0003	0.5	7
Reg 2	4000	40	0.4	0	0.0001	0.99	7

*Notes.* They are constrained used observations from the literature (see the text). 'line' characterizes the parameters of the grain size distribution, defined in table 1 of Weingartner & Draine (2001).

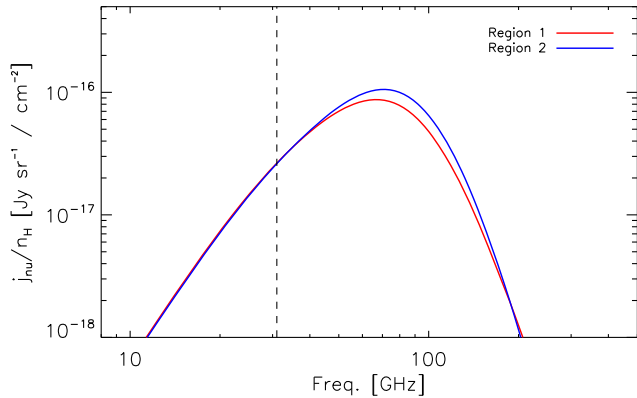


**Figure 10.** Modelled spectra using the SPDUST code for Regions 1 and 2. Table 10 lists the parameters used. The frequency of the CARMA data, 31 GHz, is marked with the vertical dashed line.

(1998) for the MC and CNM environments. It is important to note that we are interested in the *ratio* of the emissivities calculated by SPDUST; therefore, the absolute value of the parameters listed in Table 10 is not as critical as the ratio between them.

Fig. 10 shows the resulting spectra for Regions 1 and 2. The two spectra are very similar, with a fractional difference of only 21 per cent at the peak of the curves and almost zero at 31 GHz. This is expected as there are little differences in the parameters that define the spectrum for each region, and shows that it is not possible to explain the differences in emissivity relying only on environmental variations.

In SPDUST, the number of PAH is characterized by the grain size distribution defined in Weingartner & Draine (2001), and it is proportional to the total carbon abundance. By changing the 'line' parameter in the SPDUST parameters, we increased the carbon abundance of a factor of 6, to see if that can reproduce the differences in emissivity. Fig. 11 shows the resulting spectra. At 31 GHz, the ratio of the models is 5.5, very close to the measured ratio of 5.8.

Given the proximity of Regions 1 and 2, it is difficult to explain a change in carbon abundance by a factor of 6. An alternative would be increasing the number of PAHs without modifying the total amount of carbon. In Weingartner & Draine (2001), the carbonaceous grains size distribution shows two 'bumps' in the small-size regime. These bumps represent PAHs with less than  $\sim 10^3$  atoms. This means that in the SPDUST model, the number of PAHs is characterized by the relative size of these bumps. We modified the SPDUST code to allow for changes of the  $b_c$  parameter, which defines the relative size of the PAH bumps in the grain size distribution, for a fixed total carbon abundance. A similar analysis has been done by Tibbs et al. (2016). In Weingartner & Draine (2001), the quoted values for the amplitude

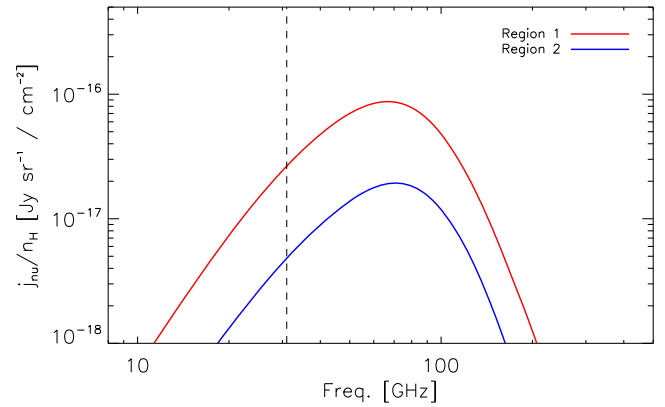


**Figure 11.** SD spectra for Regions 1 and 2, with the same parameters as in Fig. 10, but modifying the grain size distribution, with a larger total carbon abundance. Here, the ratio between the spectra at 31 GHz is 5.5, similar to the measured ratio of 5.8 from the CARMA observations.

of the grain size distribution PAH bumps is  $b_c = [0.75, 0.25]$ . They found this average values by fitting the model to data from a number of clouds, so it is probable that they might be different for the best values in the LDN 1780 cloud.

We explored the parameter space within the values listed in Table 10 that are compatible with the observed emissivity for Regions 1 and 2 listed in Table 8. We find that the *only* models compatible with the observed emissivities and with the physical properties of the cloud from the literature mentioned above are the ones that have a different grain size distribution ( $b_c$  parameter). In order to match the emissivity values, we changed the  $b_c$  parameter from  $[0.75, 0.25]$  to  $[0.9, 0.1]$ ; this is a relative change in the PAH bumps from 3/1 to 9/1. This means that environmental variations alone cannot explain the emissivity variations observed by CARMA in the cloud, and a different grain size distribution between the two regions is needed.

It is important to note that Ridderstad et al. (2006) reached the same conclusion, in requiring a significant variation in the grain size distribution along the E-W axis of LDN 1780, but based on the study of infrared data and radiative transfer modelling. Here we reach the same conclusion but from a very different data set and methodology. These differences in the properties of the grains are not a surprise, given the morphological differences that the cloud show in different IR bands. Region 2, the densest and coldest part of the cloud, will have a lower fraction of PAHs than Region 1 due to their coagulation on to larger grains.

## 5 CONCLUSIONS

Following the AME detection in LDN 1780 by Vidal et al. (2011), we have revisited the cloud analysing data at two different angular resolutions:  $1^\circ$  using *Planck* and other archival radio maps, and 2 arcmin using observations from the CARMA 3.5-m array.

Using the archival radio maps, we produced an SED of the cloud on scales of  $1^\circ$  between 0.408 and 2997 GHz. The SED shows clearly the presence of AME with a  $>20\sigma$  significance. The observed AME in the SED is very well fitted using a SD model. On these angular scales, there is a significant shift of the peak of the cloud between the emission at low frequencies (23–70 GHz) versus the emission at higher frequencies (93–2997 GHz). This means that the AME in this cloud does not originate at the same location as the bulk of the thermal dust emission.

With the newly presented CARMA data, at 31 GHz with 2 arcmin angular resolution (a factor of 3 improvement with respect to the CBI data from Vidal et al. (2011)), we studied its morphological correlations with different IR templates. The best correlation occurs with the MIPS 70- $\mu\text{m}$  template, and it has a Spearman's rank  $r_s = 0.49 \pm 0.07$ . We found a similar result using data from the Cosmic Microwave Imager (CBI) in Vidal et al. (2011), where a 31-GHz map shown a better correlation with IRAS 60- $\mu\text{m}$  map. When correlating with maps that trace PAH and VSG, the IRAC 8 and 24  $\mu\text{m}$ , we found poor correlations of  $r_s = 0.14 \pm 0.06$  and  $0.21 \pm 0.06$ , respectively. However, these correlations improve significantly when we corrected the IR templates by the ISRF, where the corrected maps should be better tracers of the column density of PAHs/VSGs, as the IR emission from these grain population is also proportional to the illuminating radiation field.

We also studied emissivity (defined as  $I_{31\text{GHz}}/N_{\text{H}}$ ) variations in the 31-GHz CARMA maps. The peak of the 31-GHz emissivity does not correspond to the densest region of the cloud. We tested the SD model in order to see if it can reproduce the observed emissivity variations taking into account the environmental differences between two regions within the cloud. We concluded that the only way that the SD model can reproduced the factor of  $\sim 6$  difference in emissivity is by introducing variations in the grain size distribution within the cloud, resulting in a E–W gradient on the population of PAHs. We show that the magnetic dust emission mechanism fails to describe the 31-GHz emission due to the lack of correlation between thermal dust emission and the cm-wave data.

Due to the high number of free parameters present in the SD model, it is relatively easy to generate spectra that can reproduce the differences in emissivity within a cloud. This is important and highlights the need of constraining the larger possible number of environmental conditions on a cloud from ancillary observations. Including molecular line and other diagnostics to model the conditions in AME regions could allow to better underpin the microphysics of the SD, in particular, separating different grain populations. High-angular-resolution observations of AME sources using current and future instruments (VLA, ALMA, ngVLA, SKA) will help greatly in this respect.

## ACKNOWLEDGEMENTS

We thank Anthony Banday for very useful comments on this work. We thank Justin Jonas for allowing us the use of the 2.3-GHz map. MV acknowledges support from FONDECYT through grant 3160750. CD acknowledges funding from an STFC Advanced Fellowship, STFC Consolidated Grant (ST/L000768/1), and an ERC Starting (Consolidator) Grant (no. 307209). We acknowledge the use of the Legacy Archive for Microwave Background Data Analysis (LAMBDA). Support for LAMBDA is provided by the NASA Office of Space Science. Some of the work of this paper was done using routines from the IDL Astronomy User's Library.<sup>3</sup> Some of the results in this paper have been derived using the HEALPix (Górski et al. 2005) package. Support for CARMA construction was derived from the Gordon and Betty Moore Foundation, the Kenneth T. and Eileen L. Norris Foundation, the James S. McDonnell Foundation, the Associates of the California Institute of Technology, the University of Chicago, the states of California, Illinois, and Maryland, and the National Science Foundation. CARMA development and operations were supported by the National Science

Foundation under a cooperative agreement, and by the CARMA partner universities.

## REFERENCES

- Ali-Haïmoud Y., Hirata C. M., Dickinson C., 2009, *MNRAS*, 395, 1055  
 AMI Consortium et al., 2009, *MNRAS*, 400, 1394  
 Battistelli E. S. et al., 2015, *ApJ*, 801, 111  
 Battistelli E. S. et al., 2019, *ApJ*, 877, L31  
 Bennett C. L. et al., 2013, *ApJS*, 208, 20  
 Bertin E., Arnouts S., 1996, *A&AS*, 117, 393  
 Casassus S. et al., 2008, *MNRAS*, 391, 1075  
 Casassus S., Cabrera G. F., Förster F., Pearson T. J., Readhead A. C. S., Dickinson C., 2006, *ApJ*, 639, 951  
 Castellanos P. et al., 2011, *MNRAS*, 411, 1137  
 Condon J. J., Cotton W. D., Greisen E. W., Yin Q. F., Perley R. A., Taylor G. B., Broderick J. J., 1998, *AJ*, 115, 1693  
 Cornwell T. J., Evans K. F., 1985, *A&A*, 143, 77  
 Dickinson C. et al., 2009, *ApJ*, 690, 1585  
 Dickinson C. et al., 2010, *MNRAS*, 407, 2223  
 Dickinson C. et al., 2018, *New Astron. Rev.*, 80, 1  
 Dickinson C., Davies R. D., Bronfman L., Casassus S., Davis R. J., Pearson T. J., Readhead A. C. S., Wilkinson P. N., 2007, *MNRAS*, 379, 297  
 Draine B. T., 2011, *Physics of the Interstellar and Intergalactic Medium*. Princeton Univ. Press, Princeton, NJ  
 Draine B. T., Hensley B., 2012, *ApJ*, 757, 103  
 Draine B. T., Lazarian A., 1998, *ApJ*, 508, 157  
 Draine B. T., Lazarian A., 1999, *ApJ*, 512, 740  
 Erickson W. C., 1957, *ApJ*, 126, 480  
 Finkbeiner D. P., Schlegel D. J., Frank C., Heiles C., 2002, *ApJ*, 566, 898  
 Fixsen D. J., 2009, *ApJ*, 707, 916  
 Franco G. A. P., 1989, *A&A*, 223, 313  
 Gaustad J. E., McCullough P. R., Rosing W., Van Buren D., 2001, *PASP*, 113, 1326  
 Górski K. M., Hivon E., Banday A. J., Wandelt B. D., Hansen F. K., Reinecke M., Bartelmann M., 2005, *ApJ*, 622, 759  
 Greaves J. S., Scaife A. M. M., Frayer D. T., Green D. A., Mason B. S., Smith A. M. S., 2018, *Nat. Astron.*, 2, 662  
 Haslam C. G. T., Salter C. J., Stoffel H., Wilson W. E., 1982, *A&AS*, 47, 1  
 Hauser M. G. et al., 1998, *ApJ*, 508, 25  
 Hensley B. S., Draine B. T., Meisner A. M., 2016, *ApJ*, 827, 45  
 Hoang T., Lazarian A., 2012, *ApJ*, 761, 96  
 Hoang T., Lazarian A., 2016, *ApJ*, 821, 91  
 Hoang T., Draine B. T., Lazarian A., 2010, *ApJ*, 715, 1462  
 Hoang T., Nguyen-Quynh L., Nguyen-Anh V., Kim Y.-J., 2018, *ApJ*, 862, 13  
 Högbom J. A., 1974, *A&AS*, 15, 417  
 Jonas J. L., Baart E. E., Nicolson G. D., 1998, *MNRAS*, 297, 977  
 Laureijs R. J., Fukui Y., Helou G., Mizuno A., Imaoka K., Clark F. O., 1995, *ApJS*, 101, 87  
 Leitch E. M., Readhead A. C. S., Pearson T. J., Myers S. T., 1997, *ApJ*, 486, L23+  
 Markwardt C. B., 2009, in Bohlender D. A., Durand D., Dowler P., eds, *ASP Conf. Ser. Vol. 411, Astronomical Data Analysis Software and Systems XVIII*. Astron. Soc. Pac., San Francisco, p. 251  
 Mathis J. S., Mezger P. G., Panagia N., 1983, *A&A*, 128, 212  
 Mattila K., Sandell G., 1979, *A&A*, 78, 264  
 Montier L., Plaszczyński S., Levrier F., Tristram M., Alina D., Ristorcelli L., Bernard J. P., Guillet V., 2015, *A&A*, 574, A136  
 Murphy E. J. et al., 2010, *ApJ*, 709, L108  
 Murphy E. J., Linden S. T., Dong D., Hensley B. S., Momjian E., Helou G., Evans A. S., 2018, *ApJ*, 862, 7  
 Pilbratt G. L. et al., 2010, *A&A*, 518, L1  
 Planck Collaboration et al., 2011a, *A&A*, 536, A1  
 Planck Collaboration et al., 2011b, *A&A*, 536, A20  
 Planck Collaboration et al., 2011c, *A&A*, 536, A25  
 Planck Collaboration et al., 2013a, *A&A*, 571, 37

<sup>3</sup><http://idlastro.gsfc.nasa.gov/>

- Planck Collaboration et al., 2013b, *A&A*, 571, 22  
 Planck Collaboration et al., 2013c, *A&A*, 565, 28  
 Planck Collaboration et al., 2016a, *A&A*, 594, A1  
 Planck Collaboration et al., 2016b, *A&A*, 594, A9  
 Planck Collaboration et al., 2016c, *A&A*, 594, A13  
 Planck Collaboration et al., 2016d, *A&A*, 594, A25  
 Reich W., 1982, *A&AS*, 48, 219  
 Reich P., Reich W., 1986, *A&AS*, 63, 205  
 Reich P., Testori J. C., Reich W., 2001, *A&A*, 376, 861  
 Remazeilles M., Dickinson C., Banday A. J., Bigot-Sazy M.-A., Ghosh T., 2015, *MNRAS*, 451, 4311  
 Ridderstad M., Juvela M., Lehtinen K., Lemke D., Liljeström T., 2006, *A&A*, 451, 961  
 Sault R. J., Teuben P. J., Wright M. C. H., 1995, in Shaw R. A., Payne H. E., Hayes J. J. E., eds, *ASP Conf. Ser. Vol. 77, Astronomical Data Analysis Software and Systems IV*. Astron. Soc. Pac., San Francisco, p. 433  
 Scaife A. M. M. et al., 2010, *MNRAS*, 403, L46  
 Silsbee K., Ali-Haïmoud Y., Hirata C. M., 2011, *MNRAS*, 411, 2750  
 Snow T. P., McCall B. J., 2006, *ARA&A*, 44, 367  
 Tibbs C. T. et al., 2011, *MNRAS*, 418, 1889  
 Tibbs C. T. et al., 2016, *MNRAS*, 456, 2290  
 Todorović M. et al., 2010, *MNRAS*, 406, 1629  
 Toth L. V., Haikala L. K., Liljestroem T., Mattila K., 1995, *A&A*, 295, 755  
 Vidal M. et al., 2011, *MNRAS*, 414, 2424  
 Vidal M., Leahy J. P., Dickinson C., 2016, *MNRAS*, 461, 698  
 Wardle J. F. C., Kronberg P. P., 1974, *ApJ*, 194, 249  
 Watson R. A., Rebolo R., Rubiño-Martín J. A., Hildebrandt S., Gutiérrez C. M., Fernández-Cerezo S., Hoyland R. J., Battistelli E. S., 2005, *ApJ*, 624, L89  
 Weingartner J. C., Draine B. T., 2001, *ApJ*, 548, 296  
 Witt A. N., Gold B., Barnes F. S., III, DeRoo C. T., Vijn U. P., Madsen G. J., 2010, *ApJ*, 724, 1551  
 Ysard N., Miville-Deschênes M. A., Verstraete L., 2010, *A&A*, 509, L1  
 Ysard N., Juvela M., Verstraete L., 2011, *A&A*, 535, A89

This paper has been typeset from a  $\text{\TeX}/\text{\LaTeX}$  file prepared by the author.